

# Suppression of surface-related loss in a gated semiconductor microcavity

Daniel Najar,<sup>1</sup> Natasha Tomm,<sup>1</sup> Alisa Javadi,<sup>1</sup> Alexander R. Korsch,<sup>2</sup> Benjamin Petrak,<sup>1</sup> Daniel Riedel,<sup>1</sup> Vincent Dolique,<sup>3</sup> Sascha R. Valentin,<sup>2</sup> Rüdiger Schott,<sup>2</sup> Andreas D. Wieck,<sup>2</sup> Arne Ludwig,<sup>2</sup> and Richard J. Warburton<sup>1, a)</sup>

<sup>1)</sup>Department of Physics, University of Basel, Klingelbergstrasse 82, CH-4056 Basel, Switzerland

<sup>2)</sup>Lehrstuhl für Angewandte Festkörperphysik, Ruhr-Universität Bochum, D-44780 Bochum, Germany

<sup>3)</sup>Laboratoire des Matériaux Avancés (LMA), IN2P3/CNRS, Université de Lyon, F-69622 Villeurbanne, Lyon, France

(Dated: 11 April 2022)

We present a surface passivation method that reduces surface-related losses by almost two orders of magnitude in a highly miniaturized GaAs open microcavity. The microcavity consists of a curved dielectric distributed Bragg reflector (DBR) with radius  $\sim 10\text{ }\mu\text{m}$  paired with a GaAs-based heterostructure. The heterostructure consists of a semiconductor DBR followed by an n-i-p diode with a layer of quantum dots in the intrinsic region. Free-carrier absorption in the highly doped n- and p-layers is minimized by positioning them close to a node of the vacuum electromagnetic-field. The surface, however, resides at an anti-node of the vacuum field and results in significant loss. These losses are much reduced by surface passivation. The strong dependence on wavelength implies that the surface passivation works by reducing the surface electric field, thereby reducing below-bandgap absorption via the Franz-Keldysh effect. These results are important in other nano-photonic devices which rely on a GaAs-vacuum interface to confine the electromagnetic field.

## I. INTRODUCTION

Concepts in cavity quantum-electrodynamics (QED) can be implemented using semiconductors. A semiconductor based microcavity can be created using a micropillar<sup>1–3</sup>, a photonic crystal cavity<sup>4,5</sup>, a whispering-gallery resonator<sup>6</sup>, and an open microcavity<sup>7–9</sup>. Quantum dots within these structures mimic atoms. In the limit of a single quantum dot (QD), a single-photon source can be realized by exploiting the weak-coupling regime of cavity-QED<sup>10</sup>. The strong-coupling regime of cavity-QED has been accessed with three different microcavity platforms<sup>1,4,9</sup>.

In all these semiconductor-based applications of cavity-QED, minimizing the absorption and scattering losses in the microcavity is very important. For single-photon sources operating in the weak-coupling regime, an efficient photon extraction from the microcavity is essential<sup>2,3</sup>. In the strong-coupling regime, a coherent exchange between an exciton in the QD and a photon in the micro-cavity is only possible if the exciton-photon coupling exceeds the rate of photon loss. Typically, this requires the development of low-mode volume, high  $Q$ -factor microcavities. A recurring theme in the development of such microcavities is the role of the GaAs surface. At the semiconductor surface, the symmetry of the lattice is broken. The GaAs surface is quite complex – there are a number of possible surface reconstructions, and a thin oxide layer typically forms on exposure to air. Reducing surface-related absorption is crucial in the development of GaAs-based cavity-QED.

Recently, considerable success in implementing cavity-

QED was reported with a QD in an open microcavity<sup>7–9,11</sup>. The “bottom” mirror is a semiconductor distributed Bragg reflector (DBR), the “top” mirror a curved, dielectric DBR. The position of the bottom mirror can be tuned *in situ* with respect to the top mirror, allowing a single QD to be brought into resonance with the microcavity mode. In the latest developments, the QDs are embedded in an n-i-p diode<sup>9,11</sup>. Both n- and p-doped GaAs result in free-carrier absorption<sup>12</sup>. To minimize the absorption within the microcavity, the n- and p-doped layers are made as thin as possible and are positioned close to the node of the vacuum electric field. This technique, positioning an absorbing layer at a vacuum field node, can also be used to reduce losses at the GaAs surface. But in this case, it involves a serious compromise. If there is a node at the surface, the largest vacuum electric field lies in the vacuum-gap and not in the GaAs material on account of interferences in the device. This reduces considerably the coupling of a QD to the vacuum electric field. An acceptably large coupling is only possible if there is a vacuum field anti-node at the surface. Success with the n-i-p devices in an open microcavity was only possible after passivating the surface<sup>9,11</sup>. The role played by the passivation is elucidated here.

We probe the surface-related absorption in a GaAs open microcavity. The main diagnostic tool is a measurement of the wavelength dependence of the  $Q$ -factor. With an untreated surface, we find that the  $Q$ -factor is modest, approximately  $10^4$  at the stopband center, much lower than the value expected from the mirror designs. Following surface passivation, we find that the  $Q$ -factor increases to  $\simeq 10^6$  at the stopband center, close to the value expected from the mirror designs. This shows that, first, the dominant loss mechanism in the untreated case is related to the GaAs surface, and second, that surface passivation remedies this loss. For the untreated surface,

<sup>a)</sup>Electronic mail: richard.warburton@unibas.ch

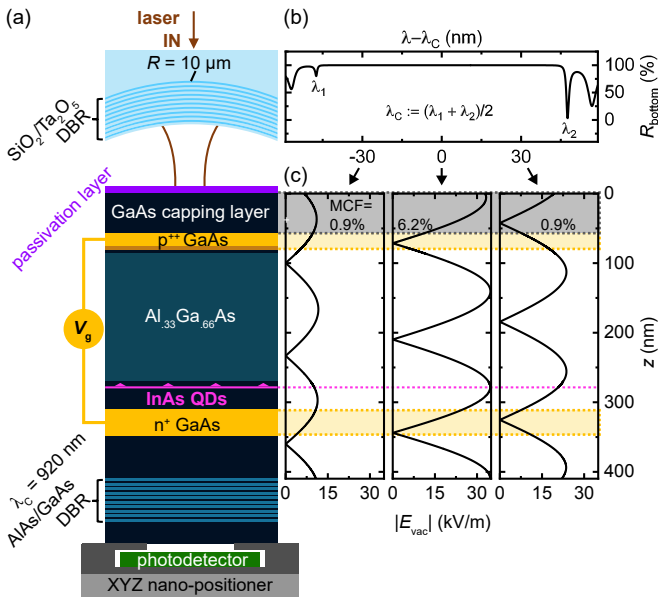


FIG. 1. Ultrahigh  $Q$ -factor optical microcavity as sensitive probe of surface-related absorption. (a) Schematic of the microcavity involving a curved dielectric-DBR and an n-i-p heterostructure with self-assembled InAs QDs on top of a semiconductor DBR (“nip-DBR”). (b) Simulated reflectance of the nip-DBR with stopband (SB) center  $\lambda_C = 920$  nm. (c) Calculated vacuum-field amplitude across the heterostructure for three different wavelengths ( $-30, 0, +30$ ) nm with respect to the SB center. As the antinodes of the vacuum-field shift in position with wavelength thereby changing the modal confinement factor (MCF) in the GaAs capping layer, surface-related absorption in the capping layer ( $10^{-10}\text{--}10^{-8}\text{ cm}^{-1}$ ) can be probed via the microcavity by measuring its  $Q$ -factor across the SB. Note that at  $\lambda_C$ , where the coupling to the QDs is maximized, free-carrier absorption in the highly doped p- and n-gates is minimized by placing them close to a vacuum-field node. Note also that the highly reduced vacuum-field at  $\lambda - \lambda_C = -30$  nm arises as at this wavelength, the largest vacuum electric-field is located in the vacuum gap.

the  $Q$ -factor has a very strong dependence on wavelength, increasing rapidly on tuning to lower wavelengths. By comparing the  $Q$ -factor to the result of model calculations, we find that we can account quantitatively for the  $Q$ -factor by ascribing the loss to absorption in the capping layer, the final 55-nm-thick GaAs layer of the heterostructure. The absorption in the capping layer is an exponential function of the photon energy, pointing to Franz-Keldysh-like absorption induced by a strong electric field at the surface<sup>13–17</sup>. In turn, this demonstrates the important role of the surface passivation layer in this device: it reduces the surface electric field, thereby much reducing the Franz-Keldysh (F-K) absorption. The standard analytic result for the F-K effect describes the absorption at the unpassivated surface but with an electric field much higher than in the standard picture (mid-gap pinning).

## II. THE OPEN, TUNABLE MICROCAVITY

The microcavity<sup>7,18</sup> consists of a curved dielectric DBR – the template is produced by CO<sub>2</sub>-laser ablation<sup>19</sup> – paired with an “nip-DBR” semiconductor heterostructure. The InAs QDs are embedded in the intrinsic part of the n-i-p diode; the diode resides on top of a semiconductor DBR, Fig. 1(a). The dielectric DBR is composed of 22 pairs of SiO<sub>2</sub>( $\lambda/4$ ) and Ta<sub>2</sub>O<sub>5</sub>( $\lambda/4$ ) (where  $\lambda$  depicts the wavelength in each material) and is terminated with SiO<sub>2</sub>. The stopband (SB) center<sup>20</sup> is 973 nm. The semiconductor DBR consists of 46 pairs of AlAs( $\lambda/4$ ) and GaAs( $\lambda/4$ ). The heterostructure is a 1.5 $\lambda$ -layer of GaAs including doped layers acting as top-gate (p<sup>++</sup>,  $10^{19}\text{ cm}^{-3}$ ) and back-gate (n<sup>+</sup>,  $2 \cdot 10^{18}\text{ cm}^{-3}$ ). The QD layer is placed at an antinode of the vacuum electric field (at a distance  $\lambda$  below the surface). The intrinsic region between QDs and back-gate acts as tunnel barrier for electrons and ensures that the QDs operate under Coulomb blockade at low temperature<sup>21</sup>. Using a piezo-based XYZ nano-positioner, the microcavity features full *in situ* tunability at cryogenic temperatures.

A measurement of the  $Q$ -factor across the SB of the nip-DBR (Fig. 1(b)) reveals possible sources of loss in the heterostructure due to the fact that the standing wave inside the cavity shifts with wavelength (Fig. 1(c)). For instance, losses in the capping layer depend on the exact wavelength: at a wavelength-detuning of ( $-30, 0, 30$ ) nm with respect to the nip-DBR’s SB center, the calculated modal confinement factor (MCF<sup>22</sup>) of the capping layer is (0.9%, 6.2%, 0.9%), respectively. Therefore, if the dominant loss mechanism in the microcavity takes place within the capping layer then the change in MCF will result in a strong dependence of the  $Q$ -factor across the stopband. Furthermore, by characterizing the mirrors carefully and by simulating the entire structure with transfer-matrix calculations, measurements of the  $Q$ -factor not only reveal the location of the dominant loss process but can also be used to determine the loss quantitatively.

## III. GaAs SURFACE PASSIVATION

Surface passivation of GaAs replaces the native oxide with a thin Al<sub>2</sub>O<sub>3</sub> layer<sup>6,23</sup>. The surface passivation recipe follows in part one of the procedures described in Ref.<sup>24</sup>. As a first cleaning step, the processed semiconductor sample (already containing Au contact pads) is successively immersed in acetone, isopropanol and ethanol inside an ultrasonic bath at  $T = 40^\circ\text{C}$ . To prevent surface treatment of the contact pads, they are covered by a manually applied drop of photoresist (AZ1512HS, Microchemicals GmbH) and baked for 10 min at  $T = 100^\circ\text{C}$ . At room temperature, the sample is dipped into an HCl solution (25%) for 1 min in order to remove the native oxide<sup>24</sup>. The sample is then rinsed with deionized water for  $\sim 1$  s and immediately immersed

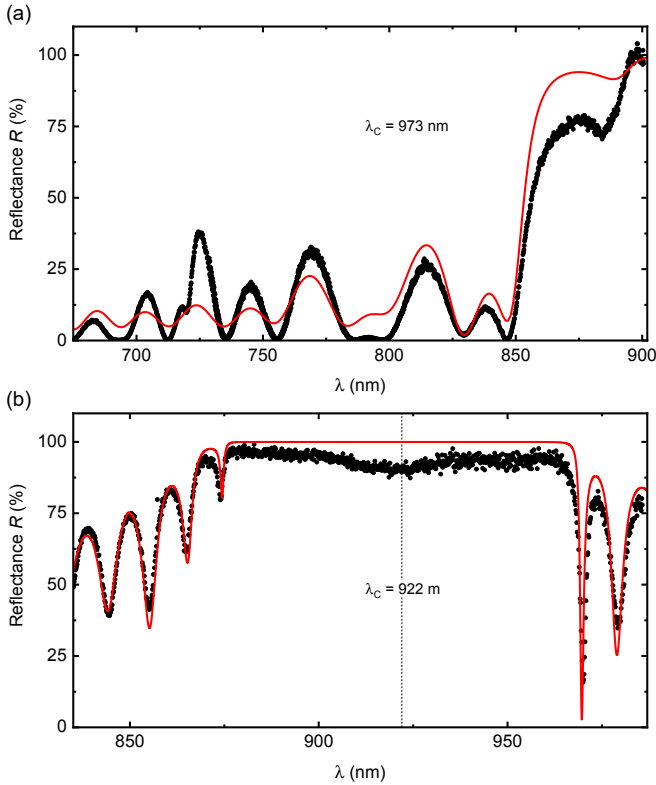


FIG. 2. Mirror characterization via reflection measurements. Each mirror is investigated at  $T = 4.2 \text{ K}$  by recording the spectrum of white light (fiber-coupled broadband illumination, either from a white light-emitting-diode or halogen lamp) reflected off the sample using a dark-field confocal microscope<sup>25</sup>. Via 1D transfer matrix methods (Essential Macleod), the designed layer thicknesses can be refined to fit the experimentally observed oscillations. (a) Dielectric DBR with 22 pairs of  $\text{SiO}_2/\text{Ta}_2\text{O}_5$ , terminated with  $\text{SiO}_2$ , as used for the curved mirror. The reflected signal is recorded on a flat surface away from the curved part of the mirror and normalized by the white-light spectrum. (b) Unpassivated nip-DBR. Here, the reflectance spectrum is obtained by normalizing the reflected signal from the mirror by the reflected signal from a Au contact pad (by moving the piezo-nanopositioner laterally by a few microns).

in an  $(\text{NH}_4)_2\text{S}$  solution (20%) for 10 min. Without rinsing the sample, it is blown dry with nitrogen and immediately transferred into an atomic-layer deposition (ALD) chamber (Savannah 100, Cambridge NanoTech Inc.).

The following ALD recipe is chosen to deposit  $\sim 8 \text{ nm}$  of  $\text{Al}_2\text{O}_3$  onto the sample surface:  $T = 150 \text{ }^\circ\text{C}$ , first pulse 50 ms (water), wait 12 s, second pulse 40 ms (TMA), wait 10 s; the cycle is repeated 80 times. The  $\text{Al}_2\text{O}_3$  layer acts as diffusion barrier for oxygen<sup>26</sup>, thus preventing reoxidation of the etched GaAs surface.

After surface passivation, the remaining challenge is to remove the photoresist that has been cross-linked due to the high temperature,  $T = 150 \text{ }^\circ\text{C}$ , inside the ALD chamber. The use of  $N$ -methyl-2-pyrrolidone (NMP) at elevated temperatures was shown to remove success-

fully the cross-linked photoresist. The sample is immersed in NMP for 9–20 h (20 h yielded a better result) at  $T = 40 \text{ }^\circ\text{C}$  and then successively cleaned for 5 min in NMP, acetone, isopropanol and methanol inside an ultrasonic bath at  $T \sim 56 \text{ }^\circ\text{C}$ . As a final step, a polymeric strip coating (First Contact, Photonic Cleaning Technologies) is used to remove any final residues from the sample surface.

#### IV. INDIVIDUAL MIRROR CHARACTERIZATION

Each DBR has a high reflectance for wavelengths within the stopband (SB). Outside the stopband, there are oscillations in the reflectivity as a function of wavelength. These oscillations are sensitive to the exact layer thicknesses in the particular mirror – this dependence is exploited to characterize the layers in each DBR.

As depicted in Fig. 2, the cavity's top and bottom mirrors are characterized at  $T = 4.2 \text{ K}$  by a broadband light-source (white light-emitting-diode or halogen lamp) and a dark-field confocal microscope<sup>25</sup>. The light from the source is coupled into a single-mode optical fiber, the output of which is collimated and focussed onto the sample surface with an objective lens (NA=0.55). Cross-polarizing elements are used in the beam path to reject all but the light reflected from the sample surface. The detection fiber is connected to a spectrometer<sup>25</sup>. The reflected light from a metallic mirror, the Au contact pad in the case of the nip-DBR, is used to record a reference spectrum. The nip-DBR's reflectance spectrum is obtained by dividing its reflected spectrum by the reference spectrum. Due to the absence of a metallic reference surface on top of the dielectric DBR in Fig. 2(a), an exponential fit of the reference spectrum from Fig. 2(b) is used instead and the maximum reflectance is normalized to one.

Via 1D transfer matrix methods (Essential Macleod, Thin Film Center Inc.) the design layer thicknesses can be refined in order to fit the reflectivity oscillations outside the stopband. The obtained models for each DBR (red solid lines in Fig. 2) provide a very convincing description of these oscillations. These mirror descriptions are then used to simulate the cavity performance, in particular the  $Q$ -factors and transmittance values at resonance as a function of the vacuum-gap between the mirrors (see Sec. IX). The slight discrepancy between the experiment and the model in Fig. 2 arises from the difficulty of recording precisely a reference spectrum for the white-light source.

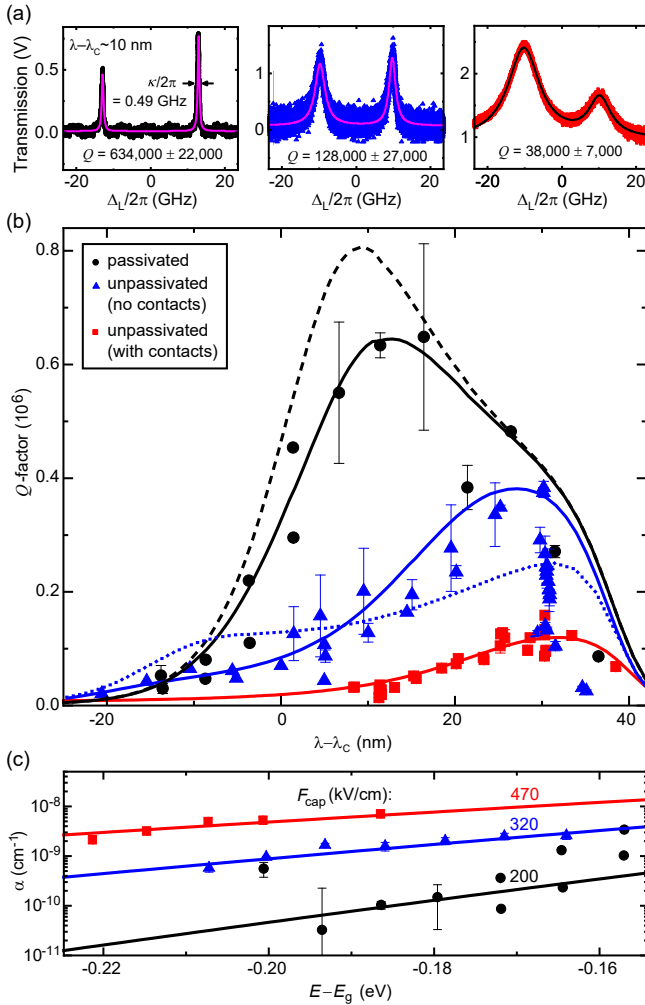


FIG. 3. Microcavity characterization via  $Q$ -factor measurements. Microcavities with three different nip-DBRs are tested at  $T = 4.2$  K: a passivated DBR with contacts (black circles), an unpassivated DBR “A” without contacts (blue triangles), and an unpassivated DBR “B” with contacts (red squares). (a) Measured transmission signal using a narrowband laser at  $\lambda - \lambda_C \sim 10$  nm as a function of laser detuning at a fixed (minimum) mirror separation. In each case, a mean  $Q$ -factor for the two longitudinal modes is determined by a double-Lorentzian fit (solid lines). (b) Evaluated  $Q$ -factors for several wavelengths. In both unpassivated cases, two (A) and six (B) datasets from similar microcavities ( $\lambda_C = 915$ –925 nm) are plotted. The solid (dashed) lines are calculated  $Q$ -factors taking into account free-carrier absorption (literature values for the absorption coefficients<sup>12</sup>) and F-K absorption<sup>16,17</sup> for electric fields  $F_{cap} = (200, 320, 470)$  kV/cm ( $F_{cap} = 0$ ).  $F_{cap}$  is the electric field in the capping layer. In order to rule out surface scattering<sup>27</sup> as the dominant absorption mechanism, the blue dotted-line indicates the calculated  $Q$ -factors taking into account a GaAs surface roughness of  $\sigma = 0.5$  nm (Fig. 5(b)) instead of F-K absorption. (c) Absorption coefficients of the capping layer. By comparing the measured and simulated  $Q$ -factors, an extinction coefficient  $k$  for the capping layer material (GaAs) can be fitted yielding an absorption coefficient  $\alpha$  via  $\alpha = 4\pi k/\lambda$ . The solid lines represent the F-K result<sup>16,17</sup> (Eqs. 1–5) using  $F_{cap}$  as fitting parameter.

## V. MICROCAVITY CHARACTERIZATION: $Q$ -FACTORS

A microcavity is constructed using passivated and unpassivated semiconductor-DBRs and a curved dielectric DBR (radius of curvature  $\sim 7$ –16  $\mu$ m) similar to the ones characterized in Fig. 2. Via narrowband-laser transmission-measurements, each microcavity is characterized by determining its  $Q$ -factor across the SB of the semiconductor DBR. The transmission signal is measured as a function of laser frequency keeping the cavity length fixed (Fig. 3(a)). To change the cavity’s resonance frequency, the mirror separation is changed by means of the Z nano-positioner.

A  $Q$ -factor is obtained for every pair of longitudinal ( $TEM_{00}$ ) modes at the minimum mirror separation ( $\sim 2$ –4  $\mu$ m, depending on wavelength and mirror-crater depth<sup>18</sup>) by fitting a double-Lorentzian. Fig. 3(a),(b) show the results for an electrically-contacted passivated sample<sup>28</sup> (black circles), an electrically-uncontacted unpassivated sample (blue triangles) as well as an electrically-contacted unpassivated sample (red squares). Without passivation, the  $Q$ -factor is around  $10^5$  for the electrically-uncontacted unpassivated sample at the SB center, and too low to measure precisely for the electrically-contacted unpassivated sample. At a red-shift of 10 nm from the SB center, the  $Q$ -factor for the electrically-contacted unpassivated sample is  $3.8 \cdot 10^4$ , and  $1.28 \cdot 10^5$  for the electrically-uncontacted unpassivated sample (Fig. 3(a)). These values are much smaller than the values expected from the DBRs – they signify that there is a significant loss mechanism. Around the SB center, where the coupling to the QD layer is maximized ( $\lambda_C = 915$ –925 nm), the  $Q$ -factors are strongly decreased by this loss mechanism – the loss reduces strongly the performance of a QD in the microcavity.

As the wavelength approaches the red-end of the SB, the  $Q$ -factors for the unpassivated samples increase. There is a pronounced asymmetry with respect to the SB center: the  $Q$ -factors fall monotonically as the wavelength shifts to the blue with respect to the SB center. These results imply that the loss mechanism is a strong function of wavelength.

After passivation, the  $Q$ -factor around the SB center increases. At a red-shift of 10 nm from the SB center, the  $Q$ -factor increases to a very large value,  $6.34 \cdot 10^5$  (Fig. 3(a)). Furthermore, the dependence of the  $Q$ -factor on wavelength is much more symmetric with respect to the SB center. In fact, the decrease on the blue-side reflects the decrease in reflectivity of the dielectric mirror which, for fabrication reasons, has a maximum reflectivity at a wavelength of 973 nm.

The passivation procedure changes the properties of the surface but leaves the rest of the microcavity unchanged. The drastic increase of the  $Q$ -factors after surface passivation leads therefore to the conclusion that the losses limiting the  $Q$ -factors of unpassivated microcavities are related to the semiconductor surface. Specifically, the loss, either an absorption or scattering mechanism,

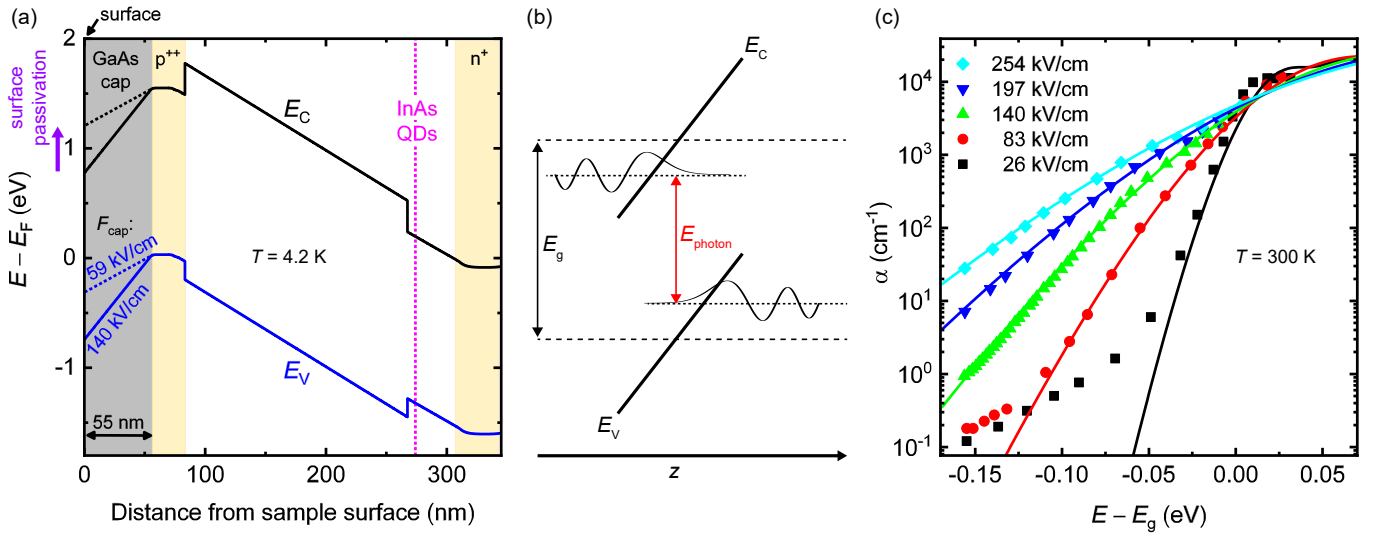


FIG. 4. Band structure and Franz-Keldysh effect. (a) Simulation of the conduction and valence bands in the n-i-p diode (nextnano) at  $T = 4.2$  K. The surface is modelled via a Schottky barrier of  $E_g/2 = 0.76$  eV reflecting the mid-gap Fermi-level pinning at the GaAs surface<sup>24</sup>. The effect of surface passivation is modelled via a reduced Schottky barrier of  $0.32$  eV to describe the experimentally observed factor of  $2.4$  reduction of the electric field in the capping layer after surface passivation. (b) Schematic of the F-K effect<sup>13,14</sup>. An electric field applied to a semiconductor allows both electrons and holes to tunnel into the forbidden energy, leading to below-gap absorption processes. (c) Room-temperature F-K absorption coefficients for different electric fields within a p-i-n double heterostructure (©2020 IEEE. Reprinted, with permission, from Ref.<sup>17</sup>). The solid lines correspond to the calculated absorption coefficients according to Ref.<sup>15,16</sup> (Eqs. 1–5).

originates at the GaAs surface itself or in the GaAs layer immediately below the surface.

To quantify the loss, the entire microcavity is modeled (see Sec. IX) using accurate descriptions of the two DBRs, including the free-carrier absorption in the doped layers in the heterostructure. Absorption is added to the capping layer (GaAs between the p-doping and the surface) and adjusted to match the experimentally determined  $Q$ -factors at each wavelength. This is a robust procedure as the surface-related loss dominates other loss channels. The extracted absorption coefficients  $\alpha$  from this procedure are plotted as a function of wavelength in Fig. 3(c).

In all three cases shown in Fig. 3(c), the absorption coefficients  $\alpha$  are extremely small. From a measurement point of view, the microcavity represents a very sensitive platform for detecting very weak absorption or scattering events. In a single-pass experiment, these losses would be very difficult to detect. Significantly, we find that  $\alpha$  depends exponentially on photon energy, a dependence that rules out scattering or broad-band absorption at the surface as these processes would have a much weaker dependence on wavelength. Instead, the exponential dependence points to below-gap absorption in an electric field.

## VI. MICROSCOPIC EXPLANATION FOR THE NIP-DBR LOSSES

We give a possible microscopic explanation for the losses in the investigated nip-DBR structure and why surface passivation significantly reduces them. In Fig. 4(a), the calculated valence- and conduction-band edges in the heterostructure are shown, a solution to the 1D Poisson equation (obtained via the nextnano software). In the unpassivated case, we simulate the mid-gap Fermi-level pinning at the surface via a Schottky barrier of  $0.76$  eV. This yields an electric field in the capping layer (“capping field”) of  $F_{\text{cap}} = 140$  kV/cm.

An electric field in a semiconductor leads to F-K absorption below the bandgap of the material<sup>13,14</sup>: owing to the position-dependence of the band-edges, the electron and hole wavefunctions can be described by Airy functions (similar to a particle in a triangular well<sup>29</sup>) and acquire an exponential tail at energies within the bandgap. The electric field therefore creates an absorption processes at photon energies  $E_{\text{photon}} < E_g$ . The situation is schematically depicted in Fig. 4(b).

According to the standard model<sup>15</sup>, F-K absorption at photon energy  $E$  due to the presence of an electric field  $F$  can be described via the absorption coefficient

$$\alpha(E, F) = \beta \cdot \frac{F^{1/3}}{E} \sum_{i=\text{lh, hh}} \left( \frac{\mu_i}{m_0} \right)^{4/3} |M_i|^2 \left( |Ai'(x_i)|^2 - x_i |Ai(x_i)|^2 \right), \quad (1)$$

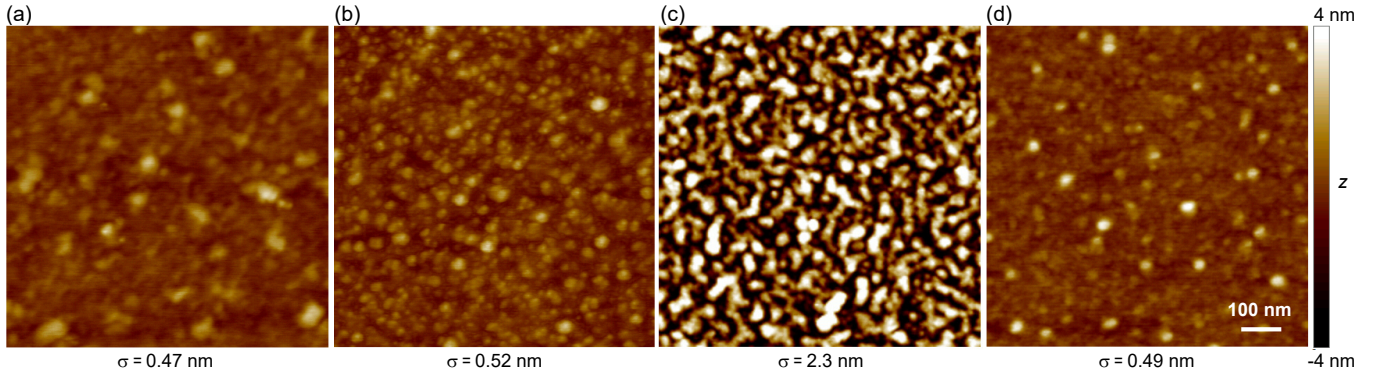


FIG. 5. Atomic force microscopy (AFM) images of different semiconductor samples. Each image depicts the same scan area of  $0.8 \times 0.8 \mu\text{m}^2$  (obtained in tapping mode) and scale bar from a height of  $-4$  to  $+4$  nm. (a) Piece of passivated bare wafer. (b) Piece of unpassivated bare wafer. (c) Unpassivated sample with contacts. (d) Piece of unpassivated bare wafer from a semiconductor DBR without n- and p-type layers. The samples in (a), (b) and (d) reveal similar root-mean-square surface roughnesses around  $\sigma = 0.5$  nm, while the sample shown in (c) exhibits a larger roughness around  $\sigma = 2$  nm.

where

$$x_i = \frac{e \cdot (E_g - E)}{\hbar\theta_i}. \quad (2)$$

$$\hbar\theta_i = \left( \frac{(eF\hbar)^2}{2\mu_i} \right)^{1/3}, \quad (3)$$

In these equations,  $\beta$  is a constant (arb. units),  $e$  is the elementary charge (in SI units),  $\hbar$  the reduced Planck's constant (in SI units),  $m_0$  the free electron rest mass (in kg),  $\mu_{\text{lh}} = 0.037m_0$  ( $\mu_{\text{hh}} = 0.058m_0$ ) the reduced mass of an electron-light-hole pair (electron-heavy-hole pair),  $F$  is given in kV/cm, the energies  $E_g$  and  $E$  in eV and  $|M_{\text{lh}}|^2$  ( $|M_{\text{hh}}|^2$ ) the momentum matrix elements for the light-hole (heavy-hole).  $\text{Ai}(z)$  is an Airy function<sup>30</sup> (with derivative  $\text{Ai}'(z)$ ).

We make use of the momentum matrix elements derived in Ref.<sup>16</sup> for different polarizations of the radiation field. For light polarized in the  $(x, y)$ -plane, the momentum matrix elements for the light- and heavy-holes read

$$|M_{\text{lh}}|^2 = P^2/3, \quad (4)$$

$$|M_{\text{hh}}|^2 = P^2, \quad (5)$$

where  $P = 0.692$  (arb. units) is a typical value for GaAs<sup>16</sup>.

We use this model for F-K absorption to describe previously reported room-temperature experiments on a p-i-n double heterostructure<sup>17</sup> (Fig. 4(c)), and extract the value of constant  $\beta$  in Eq. 1, which is found to be  $\beta = 2.5 \cdot 10^4$  (arb. units). These experiments extend to photon energies far below the bandgap, the case of interest here. There is a compelling overlap between theory and experiment.

In order to estimate F-K absorption coefficients in our n-p-DBR at 4.2 K (Fig. 3(b),(c)), we make use of Eqs. 1–5, taking the low-temperature GaAs bandgap of 1.519 eV

and  $\beta$  extracted from fitting the data in Fig. 4(c). We compare the results of the model for low-temperature F-K absorption to the experimental data presented in Fig. 3(b),(c), taking the electric field  $F$  as a fitting parameter. The exponential dependence of the absorption on the photon energy is well described with F-K absorption. However, in the unpassivated case, the capping field is a factor of 3.4 above that expected from the 1D Poisson equation (Fig. 4(a)). The origin of this discrepancy is not understood at this point, but we note several points.

First, to the best of our knowledge, there are no F-K absorption experiments reported in the literature at low temperature (4.2 K) and at photon energies far below the bandgap  $E_g$  of GaAs (at  $E - E_g \sim -0.17$  eV corresponding to  $\lambda \sim 920$  nm). Our approach here is to fit the theory presented in Ref.<sup>15,16</sup> to the room temperature experiments of Ref.<sup>17</sup> (Fig. 4(c)) and then to extrapolate the absorption coefficients to photon energies  $\sim 0.17$  eV below the bandgap. The change in temperature, from room-temperate to low temperature, is accommodated by a rigid shift in the absorption spectrum to account for the increase in the bandgap. It is conceivable that the standard F-K theory is inadequate at photon energies far below the bandgap – this point has not been tested experimentally.

Secondly, there are room-temperature experiments on F-K oscillations in doped GaAs heterostructures (a 25–80 nm thick, undoped GaAs capping layer on top of an n<sup>+</sup>-doped Al<sub>32</sub>Ga<sub>68</sub>As layer<sup>31</sup>) that also report surface electric field values a factor 1.8–3.8 above the expected ones<sup>32</sup>.

Thirdly, the F-K model describes a bulk semiconductor in a uniform electric field. Obviously, it does not take into account the microscopic details of the surface, for instance surface reconstructions and oxidation. It is possible that the details of the surface layer are important here.

In the light of this analysis, our proposal is that surface passivation reduces surface-related absorption by re-

ducing the electric field in the capping layer, thereby reducing the F-K absorption. Quantitatively, the effect of surface passivation is modelled via a reduced Schottky barrier of 0.32 eV, a factor of 2.4 reduction of the electric field in the capping layer.

A remaining question is why the bare-wafer sample without passivation shows higher  $Q$ -factors than the electrically contacted sample also without passivation (Fig. 3(b),(c)). The contacting process clearly changes the surface roughness as revealed by atomic force microscopy (AFM) measurements (tapping mode, Bruker Dimension 3100). The bare-wafer sample has a root-mean-square (rms) surface roughness of  $\sigma \sim 0.5$  nm (Fig. 5(b)). The roughness is not influenced by the high p-doping: a sample from an undoped semiconductor wafer has the same surface roughness (Fig. 5(d)). After contacting but without passivation, the surface roughness increases to  $\sigma \sim 2.3$  nm, evidence that the microscopic nature of the surface has changed. The surface roughness per se does not however account for the  $Q$ -factors of the various samples. The main point is that surface scattering does not account for the exponential dependence of the loss process on photon energy (Fig. 3(c)). A surface roughness  $\sigma$  translates into a total integrated scatter (TIS) of  $TIS \approx (4\pi\sigma/\lambda)^2$  (Ref.<sup>33</sup>) and can be modelled by an extinction coefficient  $k$  (for the 1D transfer matrix methods) according to Ref.<sup>27</sup>,

$$k = \frac{\pi(n_1 - n_2)^2(n_1 + n_2)d}{\lambda\sqrt{8(n_1^2 + n_2^2)}}, \quad (6)$$

where  $d = 2\sigma$ ,  $n_1$  and  $n_2$  are the refractive indices of the two layers surrounding the scatter layer, and  $\lambda$  is the free-space wavelength. This TIS cannot account for the  $Q$ -factor of the bare-wafer sample at the stopband center (Fig. 3(b), blue dotted-line); also, it cannot account for the strong wavelength dependence of the loss process (Fig. 3(b),(c)). Instead, we speculate that the change in GaAs surface on forming the contacts results in a change of surface pinning thereby increasing the capping field. One possibility is that the degradation of the surface on contacting spreads the available surface states to lower energies.

## VII. A SEMICONDUCTOR HETEROSTRUCTURE WITHOUT DOPING

In order to confirm that the measured losses on the heterostructure with doping are indeed a consequence of the doped layers, we compare our results to a microcavity consisting of a semiconductor heterostructure without doping. The heterostructure in this case is a  $\lambda$ -layer of GaAs (with embedded InAs QDs in the center) on top of a 33-pair AlAs/GaAs DBR<sup>7,8,34</sup>. It is a high-quality sample but may not match the ultra-high quality of the semiconductor heterostructure with doping. Initially, we repeat the mirror characterization procedure described

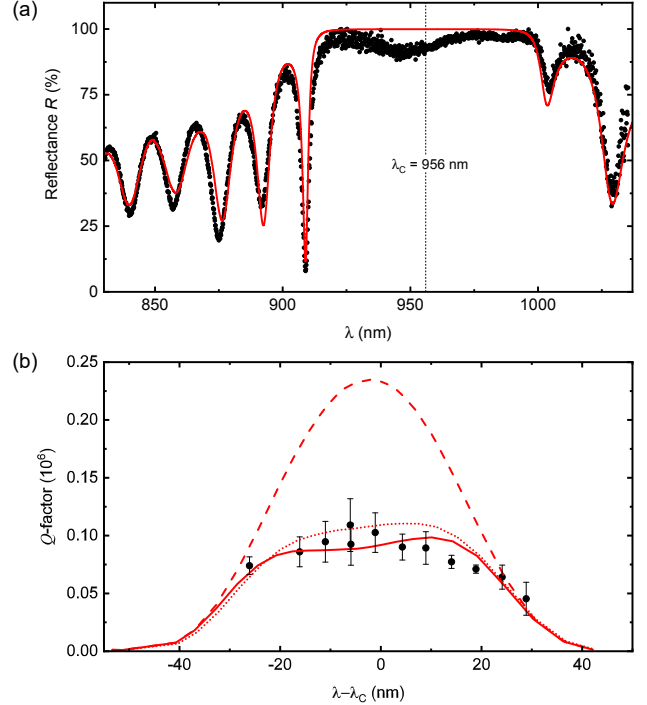


FIG. 6. Undoped semiconductor heterostructure: reflectance and  $Q$ -factor measurements. (a) Reflectance measurement of a semiconductor heterostructure without doping ( $\lambda_C = 956$  nm) at  $T = 4.2$  K. The heterostructure contains a  $\lambda$ -layer of GaAs on top of 33 pairs of AlAs( $\lambda/4$ )/GaAs( $\lambda/4$ ). A layer of QDs is included at the center of the GaAs layer. In order to record a reference spectrum, parts of the sample were covered by an Au film using electron-beam evaporation. (b)  $Q$ -factor of a microcavity at  $T = 4.2$  K consisting of this heterostructure without doping paired with a dielectric top mirror ( $\lambda_C = 973$  nm), experiment (points) and simulations. The reduction of the  $Q$ -factor around the SB center can be explained by a semiconductor surface roughness of  $\sigma = 0.5$  nm (solid line) or an interface roughness of  $\sigma = 1.0$  nm on top of every AlAs layer (dotted line). The dashed line corresponds to the case without any losses in the semiconductor DBR.

above and find a suitable model for the semiconductor layer thicknesses (Fig. 6(a)). Subsequently, we pair this mirror with the same dielectric top mirror used for the experiments on the heterostructure with doping.

Fig. 6(b) depicts the measured  $Q$ -factors as a function of wavelength for the semiconductor heterostructure without doping. The  $Q$ -factor reaches approximately  $10^5$  at the stopband center, and remains constant within measurement error over a wavelength range of approximately 20 nm. This behaviour is quite different to that of the semiconductor heterostructure with doping (Fig. 3(b),(c)). The conclusion is that the strongly wavelength dependent loss process is related to the doping.

In the absence of losses, the heterostructure-without-doping – top mirror combination should yield a  $Q$ -factor of  $2 \times 10^5$  in the stopband center, about a factor of two higher than that determined experimentally (Fig. 6(b)).

The wavelength-dependence of the  $Q$ -factor (Fig. 6(b)) is a useful diagnostic of the scattering process. We find that in this case, scattering can account for the measured  $Q$ -factors. The scattering takes place either at the sample surface or at interface roughness<sup>35</sup> at the top surface of each AlAs-layer in the DBR. Both possibilities describe the wavelength dependence of the  $Q$ -factor equally well (surface roughness alone:  $\sigma \sim 0.5$  nm (Fig. 5(d)) along with the TIS-model; interface roughness alone:  $\sigma = 1.0$  nm at the top of each AlAs layer).

The measurements on the heterostructure with doping show that surface scattering is irrelevant. This might suggest that surface scattering on the heterostructure without doping is also irrelevant. However, the surfaces may be different in the two cases and it remains an open question whether surface scattering or GaAs-on-AlAs interface scattering dominates the loss process in the heterostructure without doping. The overriding point is that scattering at a rough surface cannot reproduce the exponential wavelength dependence of the measured  $Q$ -factors using the heterostructure with doping (Fig. 3(b), blue dotted line) – the wavelength dependence of the TIS is too weak ( $\sim 1/\lambda^2$ ). Not even a model based on Rayleigh scattering (wavelength dependence  $\sim 1/\lambda^4$ ) could account for the wavelength dependence of the measured  $Q$ -factors.

## VIII. MODEL FOR THE CURVED DIELECTRIC MIRROR

An interpretation of the microcavity  $Q$ -factors in terms of losses in the semiconductor heterostructure rests on an understanding of the top mirror. The top mirror, a dielectric-DBR, is of very high quality with very low loss. To prove this point, we investigate a microcavity formed from the top dielectric-DBR and a bottom planar dielectric-DBR (at room temperature). The coatings were applied to the substrates in the same run and are nominally identical. Fig. 7 shows the measured  $Q$ -factors. At the stopband center of the top mirror ( $\lambda_C = 973$  nm), the  $Q$ -factor is extremely high,  $1.5 \cdot 10^6$ . To describe the dielectric mirror accurately at the stopband center of the semiconductor-DBR, we analyze the dependence of the dielectric-dielectric  $Q$ -factor and transmission as a function of wavelength. To describe the high transmission at short wavelengths, we are forced to red-shift the stopband center of the bottom mirror by 3 nm<sup>37</sup>. A rough interface at the “lower” surface of the five “lowest”  $Ta_2O_5$  layers shown in Fig. 1 (extinction coefficients corresponding to an interface roughness<sup>27</sup> of 0.25 nm) together with an increased absorption within the “lowest”  $Ta_2O_5$  layer (extinction coefficient  $k = 4k_{Ta_2O_5}$ , where  $k_{Ta_2O_5}$  is defined in Sec. IX) are heuristically introduced in the model in order to describe the measured  $Q$ -factors. This fit is very convincing (Fig. 7). This description of the top dielectric-mirror is used to interpret the measurements on microcavities formed using the semiconductor

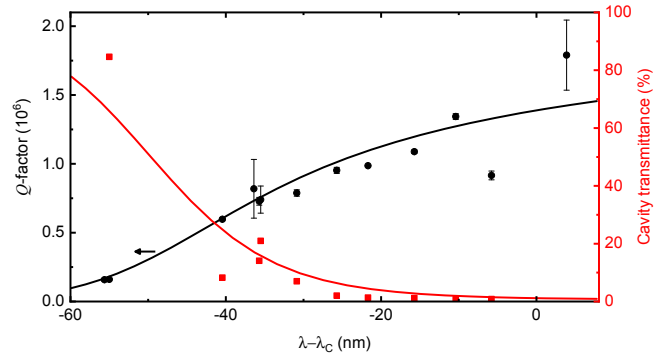


FIG. 7. Measured  $Q$ -factors and cavity transmittance of a purely dielectric microcavity. Dielectric top mirror ( $\lambda_C = 973$  nm) paired with a dielectric bottom mirror (shifted to  $\lambda_C = 976$  nm, nominally the same coating) at  $T = 300$  K. The cavity transmittance is measured by relating the transmitted power at the cavity resonance to the laser power before the objective lens multiplied by a fitted in-coupling efficiency of 59%. The black (red) solid line is a calculation of the  $Q$ -factor (cavity transmittance) taking into account a material extinction coefficient of  $k_{SiO_2} = 4 \cdot 10^{-7}$  and  $k_{Ta_2O_5} = 4.5 \cdot 10^{-7}$  for  $SiO_2$  and  $Ta_2O_5$ , respectively<sup>36</sup>. Additionally, an interface roughness of  $\sigma = 0.25$  nm above each of the five last grown  $Ta_2O_5$  layers and  $k = 4k_{Ta_2O_5}$  in the last-grown  $Ta_2O_5$  layer are introduced heuristically in order to fit the experimental data.

DBRs as bottom mirror (Fig. 3(b),(c) and Fig. 6(b)).

## IX. 1D TRANSFER MATRIX CALCULATION OF THE MICROCAVITY $Q$ -FACTORS

We list the relevant parameters used for the  $Q$ -factor calculations via a one-dimensional transfer-matrix method.

Extinction coefficients in the different materials are introduced as follows:  $k_{SiO_2} = 4 \cdot 10^{-7}$  for  $SiO_2$  (Ref.<sup>36</sup>),  $k_{Ta_2O_5} = 4.5 \cdot 10^{-7}$  for  $Ta_2O_5$  (Ref.<sup>36</sup>),  $k_{p++} = 5.2 \cdot 10^{-4}$  for  $p^{++}$ -GaAs,  $k_{p+} = 1.9 \cdot 10^{-4}$  for  $p^+$ -GaAs, and  $k_{n+} = 0.7 \cdot 10^{-4}$  for  $n^+$ -GaAs<sup>12</sup>.  $k = 4k_{Ta_2O_5}$  is used for the “lowest”, i.e. the last-grown,  $Ta_2O_5$  layer (the layer closest to the vacuum-gap) of each dielectric DBR. An extinction coefficient of  $k = \alpha_{FK}\lambda/(4\pi)$ , where  $\alpha_{FK}$  is a F-K absorption coefficient, is introduced in the capping layer;  $\alpha_{FK}$  depends on the electric field. Surface roughness is described by introducing an additional layer of thickness  $d = 2\sigma$ , where  $\sigma$  is the rms surface/interface roughness<sup>27</sup>.

In analogy to the experiment, a  $Q$ -factor is determined for a fixed “vacuum-gap” layer thickness<sup>38</sup> by calculating a cavity transmittance spectrum. A Lorentzian fit to the calculated spectrum is used to determine the resonance frequency as well as the  $Q$ -factor. This procedure is repeated for different vacuum-gaps, yielding a plot of  $Q$ -factor versus wavelength. The resulting  $Q$ -factors are presented in Fig. 3, Fig. 6 and Fig. 7.

## ACKNOWLEDGEMENTS

We thank Ivan Favero for inspiration; we thank Leonardo Midolo and Peter Lodahl for fruitful discussions. This work was funded by Swiss National Science Foundation Project 200020\_175748, NCCR QSIT and European Union Horizon2020 FET-Open Project QLUSTER. A.J. acknowledges support from the European Union Horizon 2020 Research and Innovation Programme under the Marie Skłodowska-Curie grant agreement No. 840453 (HiFig). S.R.V., R.S., A.L. and A.D.W. acknowledge gratefully support from DFH/UFA CDFA05-06, DFG TRR160, DFG project 383065199, and BMBF Q.Link.X.

- <sup>1</sup>J. Reithmaier, G. Sek, A. Löffler, C. Hofmann, S. Kuhn, S. Reitzenstein, L. Keldysh, V. Kulakovskii, T. Reinecke, and A. Forchel, “Strong coupling in a single quantum dot-semiconductor microcavity system,” *Nature* **432**, 197–200 (2004).
- <sup>2</sup>N. Somaschi, V. Giesz, L. De Santis, J. C. Loredo, M. P. Almeida, G. Hornecker, S. L. Portalupi, T. Grange, C. Anton, J. Demory, C. Gomez, I. Sagnes, N. D. Lanzillotti-Kimura, A. Lemaitre, A. Auffeves, A. G. White, L. Lanco, and P. Senellart, “Near-optimal single-photon sources in the solid state,” *Nat. Photon.* **10**, 340–345 (2016).
- <sup>3</sup>X. Ding, Y. He, Z.-C. Duan, N. Gregersen, M.-C. Chen, S. Unsleber, S. Maier, C. Schneider, M. Kamp, S. Höfling, C.-Y. Lu, and J.-W. Pan, “On-demand single photons with high extraction efficiency and near-unity indistinguishability from a resonantly driven quantum dot in a micropillar,” *Phys. Rev. Lett.* **116**, 020401 (2016).
- <sup>4</sup>T. Yoshie, A. Scherer, J. Hendrickson, G. Khitrova, H. Gibbs, G. Rupper, C. Ell, O. Shchekin, and D. Deppe, “Vacuum Rabi splitting with a single quantum dot in a photonic crystal nanocavity,” *Nature* **432**, 200–203 (2004).
- <sup>5</sup>K. Kuruma, Y. Ota, M. Kakuda, S. Iwamoto, and Y. Arakawa, “Surface-passivated high-q gaas photonic crystal nanocavity with quantum dots,” *APL Photonics* **5**, 046106 (2020).
- <sup>6</sup>B. Guha, F. Marsault, F. Cadiz, L. Morgenroth, V. Ulin, V. Berkovitz, A. Lemaitre, C. Gomez, A. Amo, S. Combrie, B. Gerard, G. Leo, and I. Favero, “Surface-enhanced gallium arsenide photonic resonator with quality factor of  $6 \times 10^6$ ,” *Optica* **4**, 218–221 (2017).
- <sup>7</sup>R. J. Barbour, P. A. Dalgarno, A. Curran, K. M. Nowak, H. J. Baker, D. R. Hall, N. G. Stoltz, P. M. Petroff, and R. J. Warburton, “A tunable microcavity,” *J. Appl. Phys.* **110**, 053107 (2011).
- <sup>8</sup>L. Greuter, S. Starosielec, A. V. Kuhlmann, and R. J. Warburton, “Towards high-cooperativity strong coupling of a quantum dot in a tunable microcavity,” *Phys. Rev. B* **92**, 045302 (2015).
- <sup>9</sup>D. Najar, I. Söllner, P. Sekatski, V. Dolique, M. C. Löbl, D. Riedel, R. Schott, S. Starosielec, S. R. Valentin, A. D. Wieck, N. Sangouard, A. Ludwig, and R. J. Warburton, “A gated quantum dot strongly coupled to an optical microcavity,” *Nature* **575**, 622–627 (2019).
- <sup>10</sup>P. Senellart, G. Solomon, and A. White, “High-performance semiconductor quantum-dot single-photon sources,” *Nat. Nanotechnol.* **12**, 1026–1039 (2017).
- <sup>11</sup>N. Tomm, A. Javadi, N. O. Antoniadis, D. Najar, M. C. Löbl, A. R. Korsch, R. Schott, S. R. Valentin, A. D. Wieck, A. Ludwig, and R. J. Warburton, “A bright and fast source of coherent single photons,” *arXiv:2007.12654* (2020).
- <sup>12</sup>H. C. Casey, D. D. Sell, and K. W. Wecht, “Concentration dependence of the absorption coefficient for n- and p-type GaAs between 1.3 and 1.6 eV,” *J. Appl. Phys.* **46**, 250–257 (1975).
- <sup>13</sup>W. Franz, “Einfluß eines elektrischen Feldes auf eine optische Absorptionskante,” *Zeitschrift für Naturforschung A* **13**, 484 (1958).
- <sup>14</sup>V. L. Keldysh, “Behaviour of non-metallic crystals in strong electric fields,” *Journal of Experimental and Theoretical Physics (USSR)* **33**, 994 (1957).
- <sup>15</sup>D. E. Aspnes, “Electric-field effects on optical absorption near thresholds in solids,” *Phys. Rev.* **147**, 554–566 (1966).
- <sup>16</sup>J. Hader, N. Linder, and G. H. Döhler, “ $k \cdot p$  theory of the Franz-Keldysh effect,” *Phys. Rev. B* **55**, 6960–6974 (1997).
- <sup>17</sup>B. Knupfer, P. Kiesel, M. Kneissl, S. Dankowski, N. Linder, G. Weimann, and G. H. Dohler, “Polarization-insensitive high-contrast GaAs/AlGaAs waveguide modulator based on the Franz-Keldysh effect,” *IEEE Photonics Technology Letters* **5**, 1386–1388 (1993).
- <sup>18</sup>L. Greuter, S. Starosielec, D. Najar, A. Ludwig, L. Duempelmann, D. Rohrer, and R. J. Warburton, “A small mode volume tunable microcavity: Development and characterization,” *Appl. Phys. Lett.* **105**, 121105 (2014).
- <sup>19</sup>D. Hunger, C. Deutsch, R. J. Barbour, R. J. Warburton, and J. Reichel, “Laser micro-fabrication of concave, low-roughness features in silica,” *AIP Adv.* **2**, 012119 (2012).
- <sup>20</sup>Note that in this work, we define the SB center as the mean value of the two wavelengths at the local minima (with  $R < 90\%$ ) of the calculated reflectance spectrum that are closest to the maximum mirror reflectance (Fig. 1(b)).
- <sup>21</sup>R. J. Warburton, C. Schaflein, D. Haft, F. Bickel, A. Lorke, K. Karrai, J. M. Garcia, W. Schoenfeld, and P. M. Petroff, “Optical emission from a charge-tunable quantum ring,” *Nature* **405**, 926–929 (2000).
- <sup>22</sup>The MCF is defined as the vacuum electromagnetic-energy confined in the layer-of-interest divided by the zero-point energy,  $\hbar\omega/2$ , i.e. the total energy of the vacuum-field mode.
- <sup>23</sup>J. Liu, K. Konthasinghe, M. Davanço, J. Lawall, V. Anant, V. Verma, R. Mirin, S. W. Nam, J. D. Song, B. Ma, Z. S. Chen, H. Q. Ni, Z. C. Niu, and K. Srinivasan, “Single self-assembled InAs/GaAs quantum dots in photonic nanostructures: The role of nanofabrication,” *Phys. Rev. Appl.* **9**, 064019 (2018).
- <sup>24</sup>Y. Xuan, H. Lin, and P. D. Ye, “Simplified surface preparation for GaAs passivation using atomic layer-deposited high- $\kappa$  dielectrics,” *IEEE Transactions on Electron Devices* **54**, 1811–1817 (2007).
- <sup>25</sup>A. V. Kuhlmann, J. Houel, A. Ludwig, L. Greuter, D. Reuter, A. D. Wieck, M. Poggio, and R. J. Warburton, “Charge noise and spin noise in a semiconductor quantum device,” *Nat. Phys.* **9**, 570–575 (2013).
- <sup>26</sup>J. Robertson, Y. Guo, and L. Lin, “Defect state passivation at III-V oxide interfaces for complementary metal-oxide-semiconductor devices,” *J. Appl. Phys.* **117**, 112806 (2015).
- <sup>27</sup>C. K. Carniglia and D. G. Jensen, “Single-layer model for surface roughness,” *Appl. Opt.* **41**, 3167–3171 (2002).
- <sup>28</sup>Note that the measured  $Q$ -factors obtained with an electrically-contacted passivated sample and with an electrically-uncontacted passivated sample were similar. The latter are not shown in Fig. 3(b).
- <sup>29</sup>J. Davies, *The Physics of Low-dimensional Semiconductors: An Introduction* (Cambridge University Press, 1997).
- <sup>30</sup>The Airy function is defined as  $Ai(z) = \frac{1}{2\pi} \int_{-\infty}^{\infty} e^{i(zt+t^3/3)} dt$ .
- <sup>31</sup>L. Zamora Peredo, L. García-González, J. Hernandez Torres, I. Cortes-Mestizo, V. Mendez-Garcia, and M. López-López, “Photoreflectance and Raman study of surface electric states on AlGaAs/GaAs heterostructures,” *J. Spectrosc.* **2016**, 1–8 (2016).
- <sup>32</sup>In order to estimate the capping fields in Ref.<sup>31</sup>, we assume mid-gap pinning, dividing half the bandgap  $E_g/2 = 0.71$  eV of GaAs at 300 K by the capping layer thicknesses there reported.
- <sup>33</sup>J. M. Bennett, “Recent developments in surface roughness characterization,” *Meas. Sci. Technol.* **3**, 1119–1127 (1992).
- <sup>34</sup>We note that the semiconductor heterostructure without doping was not grown with the same MBE as the semiconductor heterostructure with doping.

<sup>35</sup>D. E. Wohlert, K. L. Chang, H. C. Lin, K. C. Hsieh, and K. Y. Cheng, “Improvement of AlAs–GaAs interface roughness grown with high As overpressures,” *J. Vac. Sci. Technol. B: Microelectronics and Nanometer Structures Processing, Measurement, and Phenomena* **18**, 1590–1593 (2000).

<sup>36</sup>F. Beauville and The VIRGO Collaboration, “The VIRGO large mirrors: a challenge for low loss coatings,” *Class. Quantum Grav-*

*ity* **21**, S935–S945 (2004).

<sup>37</sup>We note that reflectance spectra (Fig. 2(a)) on different samples with nominally the same dielectric coating exhibited up to 6 nm shifts in wavelength, most probably due to thickness variations across the wafer.

<sup>38</sup>The minimum vacuum-gap is 1.2  $\mu\text{m}$ , limited by the depth of the microcavity craters.